IAEA
International Atomic Energy Agency

20th IAEA Fusion Energy Conference
Vilamoura, Portugal, 1 to 6 November 2004

IAEA-CN-116/EX/10-6Ra

MEASUREMENTS OF IMPURITY AND HEAT DYNAMICS DURING NOBLE GAS JET-INITIATED FAST PLASMA SHUTDOWN FOR DISRUPTION MITIGATION IN DIII-D

E.M. HOLLMANN[1], T.C. JERNIGAN[2], M. GROTH[3], D.G. WHYTE[4], D.S. GRAY[1], D.P. BRENNAN[5], N.H. BROOKS, T.E. EVANS, D.A. HUMPHREYS, C.J. LASNIER[3], R.A. MOYER[1], A. MCCLEAN[6], P.B. PARKS, V. ROZHANSKY[7], D.L. RUDAKOV[1], E.J. STRAIT, and W.P. WEST

General Atomics
San Diego, California 92186-5608
United States of America

[1]University of California, San Diego, La Jolla, California USA
[2]Oak Ridge National Laboratory, P.O. Box 2008, Oak Ridge, Tennessee, USA
[3]Lawrence Livermore National Laboratory, Livermore, California, USA
[4]University of Wisconsin, Madison, Wisconsin, USA
[5]Massachusetts Institute of Technology, Boston, Massachusetts, USA
[6]University of Toronto Institute for Aerospace Studies, Toronto, Canada
[7]St. Petersburg State Polytechnical University, St. Petersburg, Russia

Measurements of Impurity and Heat Dynamics During Noble Gas Jet-Initiated Fast Plasma Shutdown for Disruption Mitigation in DIII-D

E.M. Hollmann[1], T.C. Jernigan[2], M. Groth[3], D.G. Whyte[4], D.S. Gray[1], D.P. Brennan[5], N.H. Brooks[6], T.E. Evans[6], D.A. Humphreys[6], C.J. Lasnier[3], R.A. Moyer[1], A.G. McLean[7], P.B. Parks[6], V. Rozhansky[8], D.L. Rudakov[1], E.J. Strait[6], and W.P. West[6]

[1]University of California, San Diego, La Jolla, CA 92093-0417, USA
[2]Oak Ridge National Laboratory, P.O. Box 2008, Oak Ridge, TN 37831, USA
[3]Lawrence Livermore National Laboratory, Livermore, CA 94551, USA
[4]University of Wisconsin, Madison, WI 53706, USA
[5]Massachusetts Institute of Technology, Boston, MA 02139, USA
[6]General Atomics, P.O. Box 85608, San Diego, CA 92186-5608, USA
[7]University of Toronto Institute for Aerospace Studies, Toronto, M5S1A1, Canada
[8]St. Petersburg State Polytechnical University, St. Petersburg, 195251, Russia

Abstract. Impurity deposition and mixing during gas jet-initiated plasma shutdown is studied using a rapid (~2 ms), massive (~10^{22} particles) injection of neon or argon into stationary DIII-D H-mode discharges. Fast-gated camera images indicate that the bulk of the jet neutrals do not penetrate far into the plasma pedestal. Nevertheless, high (~90%) thermal quench radiated power fractions are achieved; this appears to be facilitated through a combination of fast ion mixing and fast heat transport, both driven by large-scale MHD activity. Also, runaway electron suppression is achieved for sufficiently high gas jet pressures. These experiments suggest that massive gas injection could be viable for disruption mitigation in future tokamaks even if core penetration of jet neutrals is not achieved.

1. Introduction

Avoiding the deleterious effects of disruptions on vessel walls is an important design issue for future large tokamaks. In the planned International Thermonuclear Experimental Reactor (ITER), for example, the total discharge energy content is projected to be about 1 GJ, with about half in the form of thermal energy and about half in the form of magnetic energy [1]. During a major disruption, the thermal energy is expected to impact the vessel walls on a thermal quench timescale of several ms, resulting in localized melting/sublimation of wall tiles. Then, the remaining cold plasma is expected to radiate away the magnetic energy on a current quench timescale of about 50 ms. Additional vessel damage could occur during this time from "halo currents" if the current channel contacts the conducting wall [2], and from relativistic electrons if a runaway electron beam is formed during the current quench [3].

A successful disruption mitigation technique in ITER should radiate the initial thermal energy to the walls on a timescale of order 1-10 ms; this is long enough to give tolerable wall heat loads and short enough that the resulting plasma is expected to be too cold and resistive to create significant halo currents. Simulations indicate that the deposition of sufficiently large quantities (>10^{22}/m^3) of neon or argon impurities into the core plasma of ITER can cause a radiative collapse of the thermal energy on the required timescale without generating runaway electrons [4]. Presently, two methods of impurity injection are being pursued in the tokamak community: cryogenic pellet injection and high-pressure gas jet injection. Fast shutdown, high radiated power fractions, and low halo currents have been shown to result from disruptions initiated by cryogenic argon and neon pellets in ASDEX [5], JT-60U [6], DIII-D [7], and T-10 [8]. However, significant runaway electron generation was observed, especially when using argon pellets, leading to an increased interest in high-pressure gas injection [7].

High-pressure gas injection has been shown to provide fast shutdown without the generation of significant runaway electrons in DIII-D using (separately) helium, neon, and argon gas jets [4]. Suppression of a pre-existing runaway beam was demonstrated in TEXTOR using helium [9]. In JT-60U, rapid shutdown while avoiding runaway generation was achieved ed by puffing a hydrogen-argon gas mixture; however, significant runaway

generation was observed when using argon only [10]. In JET, rapid shutdown without runaway electrons was obtained using helium, but not when using neon or argon jets [11].

Understanding the dynamics of the radiating impurities is crucial for evaluating pellet or high-pressure gas injection as potential disruption mitigation techniques. Ideally, the initial neutral deposition should be as uniform as possible to minimize the formation of large pressure gradients and magneto-hydrodynamic (MHD) instabilities, which could result in large conducted heat loads to the chamber walls [12].

Here, measurements are presented which indicate that the impurity transport during high-pressure gas injection in DIII-D is complex and can occur in several stages. The jet neutrals typically appear to stop soon after hitting the plasma edge. Impurity ions and the associated cold front then begin diffusing radially inward. When this cold front reaches sufficiently far into the plasma core, typically around $q = 2$, an explosive growth of MHD instabilities occurs. The core electron temperature collapses and an increased mixing of impurity ions occurs. Most of the plasma thermal energy is radiated away, although a complete mixing of impurity ions and hot plasma does appear to occur. Despite the large MHD, divertor and main chamber heat loads appear smaller than in normal disruptions. These results suggest that ideal, uniform deposition of neutrals may not be required for disruption mitigation in future tokamaks.

2. Experimental Layout

For the experiments discussed here, lower single null H-mode discharges were used in the DIII-D tokamak [13]. Typical experimental parameters were: toroidal magnetic field $B_\phi = 2.1$ T, plasma current $I_p = 1.5$ MA, central electron temperature $T_e = 2.5$ keV, and central electron density $n_e = 8\times10^{13}/\text{cm}^3$. At $t = 3000$ ms, these discharges where terminated by the high-pressure injection of a noble gas (usually neon or argon). This experimental technique was used to allow good shot-shot repeatability to optimize diagnosis of the jet dynamics.

Figure 1(a) shows a schematic of the gas jet hardware relative to the vacuum vessel. A $V = 1$ liter reservoir at the vessel is typically pressurized to around 50 atm with noble gas. A fast-acting solenoid then vents this reservoir into the vacuum vessel, typically releasing ~3×10^{22} particles over a 2 ms pulse. Two slightly different jet drift tube geometries are used in the experiments discussed here: an open geometry in which the gas travels down a length =1.3 m, diameter =15 cm tube to reach the vacuum chamber, and a directed geometry in which the gas travels down a length =1.3 m, diameter =1.5 cm tube. The open geometry gives good vacuum conductance, resulting in a fast characteristic rise time of the gas pressure at the plasma edge (<1 ms). The directed geometry has a longer gas pressure rise time (~2-4 ms) but has the advantage of being aimed more toward the center of the plasma.

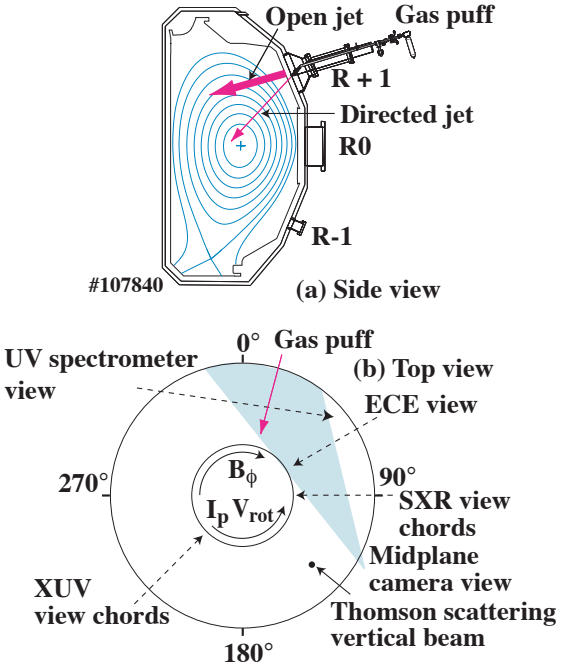

Fig. 1. Schematic of experimental layout showing (a) side view of jet geometry and (b) top view with diagnostic locations.

Figure 1(b) gives an overview of the principal diagnostics used in this work. Electron temperature is measured using Thomson scattering and electron cyclotron emission (ECE), while total radiated power is measured using an XUV photodiode array [14]. The jet UV emission spectrum is measured using a core tangential UV survey spectrometer. Each

plasma shot, one tangential, midplane-view image is obtained of the gas jet using a single frame, fast-gated CID camera.

3. Jet Neutral Dynamics

A general overview of timing of the gas jet-plasma interaction is shown in Fig. 2. At t = 3000 ms the gas jet valve is opened for about 2 ms, Fig. 2(a). After a vacuum transit time of several ms, the jet hits the edge of the plasma, Fig. 2(b). Soon afterwards, the edge electron temperature T_e collapses, Fig. 2(c), followed by the core T_e, Fig. 2(d). The rapid core T_e collapse (the thermal quench, TQ, defined here as the time period over which the core T_e falls from 90% to 10% of its initial value) is accompanied by large magnetic fluctuations, Fig. 2(e), and radiated power levels, Fig. 2(f). Finally, over a slower time of around 10 ms, the plasma current decays (the current quench, CQ), Fig. 2(g).

Figure 3(a) shows the measured vacuum transit time Δt_{vac} as a function of N_{inj}, the number of injected particles. N_{inj} is varied by varying the valve gate time between 2–3.5 ms and the reservoir pressure between 20–80 atm i.e. mostly by varying jet pressure. The data suggest that the neutrals propagate down the vacuum drift tube at between 1 and 2 times the initial (300 K) neutral sound speed. This is qualitatively consistent with previous studies of jet expansion into vacuum, which find a forward propagation speed of 1.9 times the initial neutral sound speed [15].

Figure 3(b) shows the cold front plasma transit time Δt_{pla} as a function of N_{inj}. It can be seen that, unlike the vacuum propagation, the cold front propagation through the plasma is typically longer than the sound speed time, indicating that the jet impurities have slowed down at the plasma edge. A decreasing trend in propagation time with increasing N_{inj} is evident in the data: at the largest values of N_{inj}, the average cold front propagation through the plasma is quite rapid, of order the neutral sound speed [4]. The "high T_e" data of Fig. 3 is taken with target plasmas with core electron temperature T_e = 3.6 keV (as opposed to around 2.5 keV). No significant difference in the plasma transit time is observed, however.

The data of Fig. 3 suggest that the jet neutrals expand freely down the vacuum drift tube but then slow down or stop when hitting the edge of the plasma. This is consistent with with fast-gated visible light images of the jet. Directed geometry neon gas jets were imaged using a Ne-I filter (640.2 nm), while directed argon gas jets were imaged using an Ar-I filter (696.5 nm) or an Ar-II filter (611.5 nm). Preliminary images were obtained of open geometry

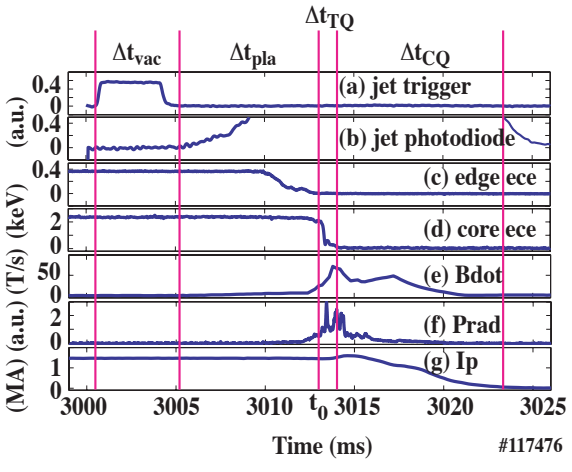

Fig. 2. Overview of gas jet-initiated disruption timing for directed argon jet showing (a) gas jet valve solenoid current, (b) visible emission from photodiode looking at jet port, (c) edge ECE emission, (d) core ECE emission, (e) magnitude of magnetic fluctuations, (f) plasma radiated power, and (g) plasma current.

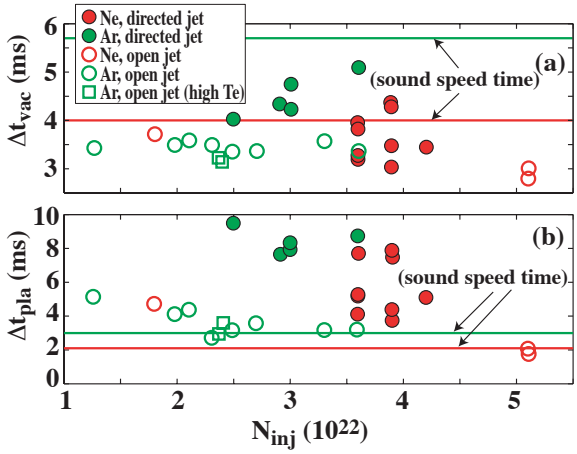

Fig. 3. (a) Noble gas vacuum transit time Δt_{vac} and (b) cold front plasma transit time Δt_{pla} as a function of number of injected particles N_{inj}.

jets in Ar-I only. The camera integration time was short (50 μs) so that the jet motion was small over the integration time. Visible spectroscopy of the jet-plasma interaction region shows that the desired lines are dominant (>95%) within the 6 nm bandpass of the camera filters.

Figure 4 shows directed argon jet images taken in (a) Ar-I and (b) Ar-II. A linear false color scale is used with yellow being the most intense. The axes indicate poloidal (θ) and toroidal (ϕ) directions. Both images are taken at the beginning of the TQ. White lines are used to show the locations of the jet port (15R+1) and neighboring ports. A dashed white line shows the expected trajectory of the central ray of a directly penetrating jet. In these disruptions, the time between the jet striking the edge of the plasma and the beginning of the TQ is about 8 ms. In this time period, we expect freely-expanding argon neutrals to have traveled about 4 m radially inward, several times the plasma minor radius. In contrast, it is clear from Fig. 4(a) that the jet neutrals have remained fairly localized to the plasma-jet strike point at 15R+1, ρ=1. For scale, the distance between the 15R+1 and 30R+1 ports is roughly 0.5 m. In Fig. 4(b) it can be seen that Ar^+ emission is elongated along the edge magnetic field direction, as expected. The angle of the ion emission band seen in Fig. 4(b) is consistent with the field line pitch in the plasma edge region, with safety factor $q \approx 4$. Quantitative interpretation of the camera images is complicated because of the line-integrated nature of the data. Qualitatively, the images demonstrate that the bulk of the jet neutrals are not penetrating to the center of the plasma. However, the dynamic range of the images is insufficient to rule out small (<1%) populations of neutrals in the center of the plasma. We do not expect significant variation in the emission efficiency (i.e. surface brightness) of the jet as it traverses the plasma, since 1-D numerical modeling of argon ablation plumes for the experimental conditions expected here indicates that the electron temperature in the neutral-plasma overlap region at the jet edge remains near T_e = 1–2 eV, even if the jet were to enter the core plasma [16].

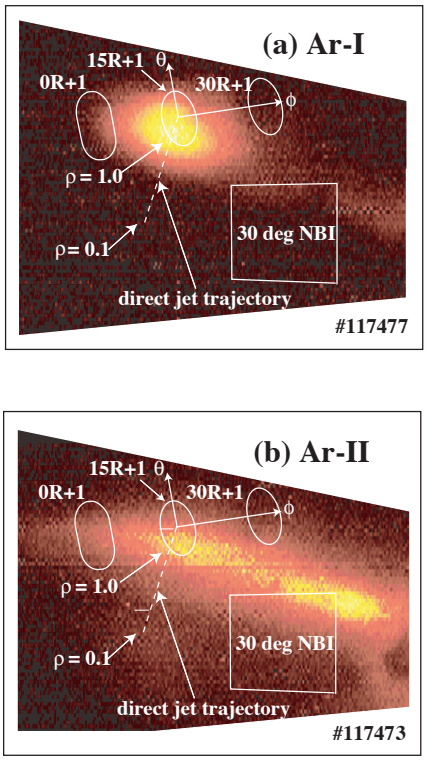

Fig. 4. (a) Ar-I and (b) Ar-II jet images taken at the beginning of the thermal quench of directed Ar-jet disruptions.

Simulations indicate that the neutral cloud is opaque to the plasma electrons [16], so the jet propagation depth is probably not set by depletion from ionization, but rather by pressure balance. For typical gas reservoir pressures (50 atm), we estimate that the jet neutral ram pressure N_oT_o at the top of the plasma pedestal edge is of order 0.1 atm, while the plasma pressure $n_e(T_e+T_i)$ is also of order 0.1 atm, the surface ablation pressure is of order 2 atm [17], and the magnetic pressure is of order 16 atm. For a neutral jet, the ablation pressure is therefore expected to be the dominant force opposing the jet propagation into the core, although the magnetic pressure could also play a role through jet surface currents.

The localization of the jet impurity neutrals to the plasma edge is also supported by Thomson scattering data. Figure 5 shows fast (burst mode) Thomson data from two repeat shots, each with a directed neon jet. Curves of electron density n_e and electron temperature T_e are plotted as a function of r/a, the radius normalized by the pre-disruption separatrix radius. Time slices are labeled relative to start of the TQ, t_0. In these disruptions, the jet hits the

plasma at roughly t_0 - 8 ms. Relative to the unperturbed plasma (t_0 - 10 ms), the TQ electron density just inside that edge pedestal r/a = 0.8 has increased a modest 13%. The seperatrix density r/a=1, however, has increased by about 2 times, and the SOL density r/a=1.05 has increased 10× over the same time period, indicating a very strong ionization source at $r/a > 1$. During the TQ ($t = t_0$ to t_0+0.4), the core plasma density actually decreases slightly. Overall, neglecting toroidal variation in n_e, this data suggests that the bulk of the impurities remain localized to $r/a > 1$.

4. Jet Ion Dynamics

Radial mixing of impurity ions can play an important role in the thermal collapse of the core. Rapid impurity ion mixing can be observed indirectly with the DIII-D XUV photodiode array, which provides fast measurement of the total radiated power along 30 view chords. Figure 6 shows the distribution of radiated power measured during the TQ of an open neon jet disruption. At the beginning of the TQ, it can be seen that the plasma radiation is confined to a small bump at the top of the array (pink curve). Mapping toroidally along unperturbed flux surfaces from the diode array (ϕ=225°) to the the gas jet (ϕ=15°) suggests that this radiation comes from impurity ions which are dominantly localized to the separatrix, *i.e.* very little inward mixing of ions has taken place by the beginning of the TQ. Shortly thereafter, by the end of the thermal quench (red curve), the peak of the radiation appears to be localized around q=2, indicating very rapid inward motion. This impurity ion mixing is not complete, however: this is indicated by the deviation between the red curve and the expected distribution for a radiating source which is homogenous over the plasma volume (dashed line).

Despite the incomplete mixing of impurity ions during the TQ, the thermal contact between the impurity ions and the hot core plasma appears to be quite good. Figure 7 shows (a) the TQ radiated energy and (b) the TQ radiated energy originating in the main chamber normalized by the total radiated energy (divertor plus main chamber), both as a function of initial stored thermal energy W_0. It can be seen that nearly unity (~90%) TQ radiated power fraction is obtained in the gas puff disruptions, with nearly 100% of this radiation coming from the main chamber. This contrasts with normal disruptions, where only 40% of the initial thermal energy is typically radiated away. In Fig. 7, the radiated energy as well as an approximate separation of main-chamber versus divertor radiation are estimated from the line-integrated XUV brightness data [18].

Data from the DIII-D core-viewing UV survey spectrometer indicate that, on average, about 90% of the thermal quench radiation comes in the form of noble gas ion line radiation, with the missing 10% being mostly carbon ion line radiation. During normal disruptions, in contrast, carbon emission is dominant (>50%). Carbon is probably sputtered from the

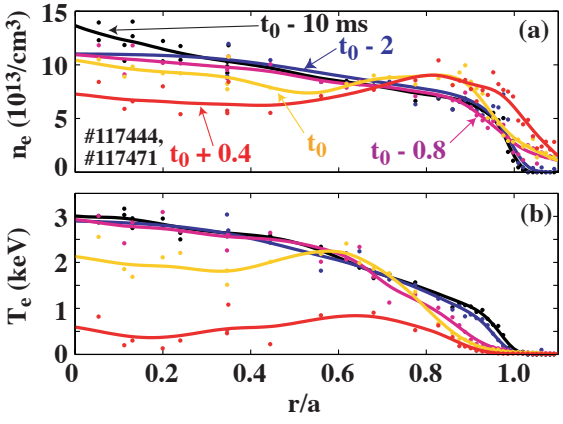

Fig. 5. Thomson scattering data of (a) electron density and (b) electron temperature as a function of normalized radius for a directed neon jet.

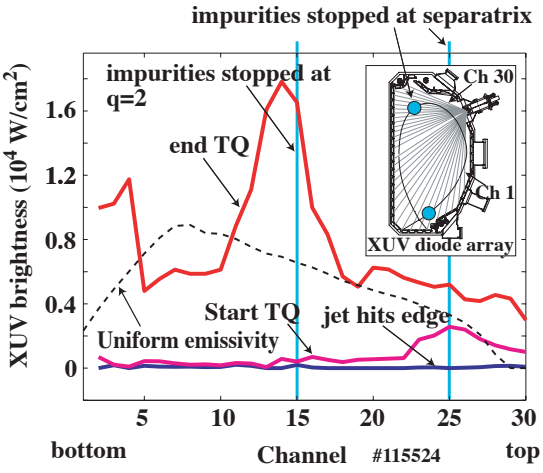

Fig. 6. Total (XUV) plasma brightness as a function of channel number for open neon jet.

graphite chamber walls and divertor during the TQ; recombination of fully-stripped carbon ions already present in the core plasma is too slow to be significant on the TQ time scale.

5. Role of Heat Transport

The fact that a very high TQ radiated energy fraction is achieved despite incomplete impurity mixing indicates that radial heat transport plays a role in connecting the hot core plasma to the radiating impurities. Evidence for rapid heat transport out of the core plasma can be seen in Fig. 5(b): for $r/a < 0.7$, an increase in n_e due to local ionization is not observed, indicating that the T_e collapse in this region is not radiative, but conductive, *i.e.* heat and particles are moving out of the core into the radiating edge region. Evidence for strong radial heat transport can also be seen in the edge data: by $t = t_0$, the electron temperature in the SOL r/a =1.05 has dropped two-fold, from 30 eV to 15 eV, but the electron pressure n_eT_e has actually increased 5-fold, so outward radial transport of heat must also be taking place across the separatrix.

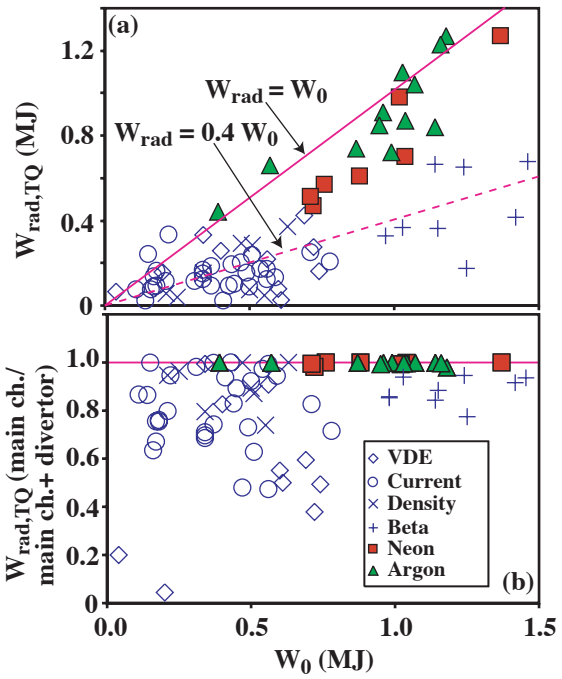

Fig. 7. (a) Thermal quench radiated power and (b) Thermal quench radiated power in main chamber divided by main chamber + divertor radiation as a function of initial stored thermal energy.

A qualitative indication of edge transport during the TQ is shown in Fig. 8, which shows ion saturation current J_{sat} from an outer midplane wall probe and plasma brightness from a main-chamber viewing XUV view chord. During a normal (current-limit) disruption, Fig. 8(a), the plasma flux to the wall arises first. The resulting sputtered carbon enters the plasma and causes the observed radiated power spike. In an open jet neon puff disruption, Fig. 8(b), the thermal quench radiation arises first, followed by an eventual plasma-wall contact. This sequence is also consistent with the observation that less carbon ion radiation is seen with the UV spectrometer in the gas puff disruptions. Fast midplane filterscope C_{III} measurements are found to correlate well with midplane probe J_{sat} measurements, confirming the expected correlation between wall plasma loads and sputtered carbon [19].

The transport of heat and particles into the main chamber wall observed in Fig. 8 is accompanied by a flow of heat along open field lines into the divertor floor. Figure 9 shows the average TQ heat load across the lower divertor floor calculated from IR camera images. Figure 9(a) shows a density-limit disruption, Fig. 9(b) a current-limit disruption, Fig. 9(c) a beta-limit disruption, Fig. 9(d) an open jet neon puff disruption, and Fig. 9(e) a type-I ELM. It can be seen that the magnitude of the divertor heat loads varies substantially depending on the type of disruption. The neon jet shutdown can be seen to have the smallest divertor heat loads of all the disruptions; this is consistent with

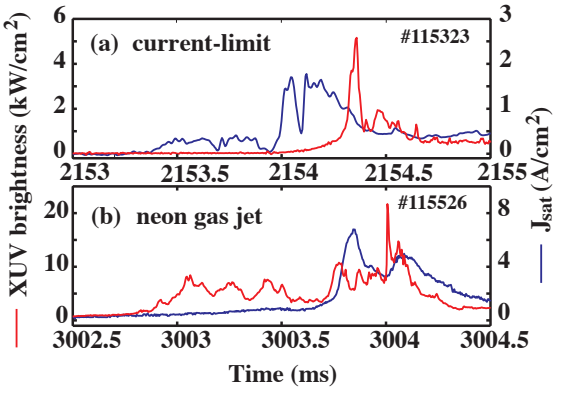

Fig. 8. Main chamber radiant brightness and outer midplane ion saturation current at wall versus time for (a) a current limit disruption and (b) a neon gas jet disruption.

the interpretation of Fig. 8(b) that much of the thermal energy is radiated away before the plasma-wall contact occurs. The dashed lines in Figs. 9(a), (b), and (d) are estimates of the divertor heat load resulting from main chamber radiation.

The red lines of Fig. 9 show the original (pre-disruption) divertor strike point locations from magnetic EFIT recon-structions. The initial strike point locations are seen to provide a reasonably good indicator of the heat load location during the ELM pulse. During disruptions, however, the heat load distribution is not well-localized to the pre-disruption strike points and does not even display good toroidal symmetry, as shown in the beta-limit disruption, where two IR camera views were available.

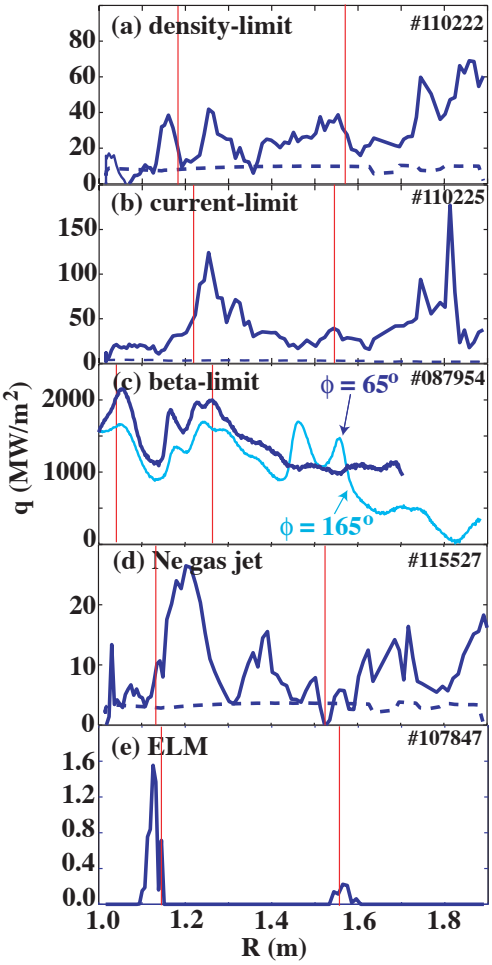

Fig. 9. Thermal quench average lower divertor heat load from IR thermography for different transient loads: (a) density limit disruption, (b) current limit disruption, (c) beta limit disruption, (d) neon gas puff disruption.

6. Role of MHD

The rapid TQ heat transport discussed in the previous section is probably the result of large-scale MHD activity. There is a variety of evidence supporting this: the large magnitude of the observed transport rate (e.g. Fig. 5 giving $\chi_\perp > 100$ m^2/s), the coincidence of the TQ radiation flash with magnetic fluctuations (e.g. Fig. 2, and strong TQ distortion of the separatrix suggested by IR thermography, Fig. 9).

Evidence for strong MHD activity during disruptions can also be seen in soft x-ray (SXR) emission: Fig. 10 shows tomographic reconstructions of the SXR emissivity contours (a) pre-disruption, (b) during the TQ, and (c) during the CQ of an open argon jet disruption. During the TQ of these disruptions, SXR emission is believed to be dominated by bremsstrahlung, so the strongly distorted contours of Fig. 10(b) indicate strong distortions of T_e contours (and magnetic flux surfaces). During the CQ, on the other hand, measured SXR emission is believed to be dominated by MeV runaway electrons striking argon ions. Figure 10(c) suggests that the large MHD activity does not result in complete destruction of the flux surfaces, since good flux surfaces are required to form a runaway electron beam (with loop voltages of order several volts, many toroidal orbits are necessary to reach MeV energies).

Typically, TQ SXR tomography, such as Fig. 10(b) indicates that the poloidal flux surface structure during the TQ is quite nonlinear, large-amplitude, and complex. Overall, though, within the limited spatial resolution of the SXR diagnostic (~10 cm), the poloidal structure appears to be relatively low-order, e.g. little evidence of very high-m poloidal structures such as ballooning filaments is seen. This is supported by wall loops, which suggest that the dominant TQ magnetic perturbation is fairly low order, with toroidal mode number n=1 and poloidal mode numbers m = 1 and 2 usually dominant. This is illustrated in Fig. 11, which shows pickup loop data from (a) poloidal and (b) toroidal current loop arrays during the TQ of an open neon jet disruption. The curves are fits to (a) m = 2 and (b) n = 1, indicating the TQ magnetic structure can be described reasonable well by m/n = 2/1. The overall negative shifts in the data of Fig. 11(a) and (b) indicate that the current channel is

shrinking and shifting inward slightly. This is observed at the onset of most gas jet disruptions and is thought to arise from the impurities cooling the plasma edge, causing a current channel shrinking plus an inward plasma shift because of the dropping plasma pressure.

Traditionally, the TQ of disruptions is associated with the growth and eventual overlap of magnetic islands [20]. However, the rapid (often ~ 0.1 ms) onset of the TQ MHD observed here seems to rule out standard resistive island growth and overlap, which is expected to require time scales of order 100 ms [21]. The low order structure and rapid growth rate seem to suggest that the plasma has approached an ideal limit, such as the $n = 1$ kink, at which point both ideal and resistive modes can grow rapidly. Simulations indicate that resistive reconnection events in narrow resonant layers can cause rapid mixing of heat and particles into the plasma center if a $n = 1$ kink is destabilized [22].

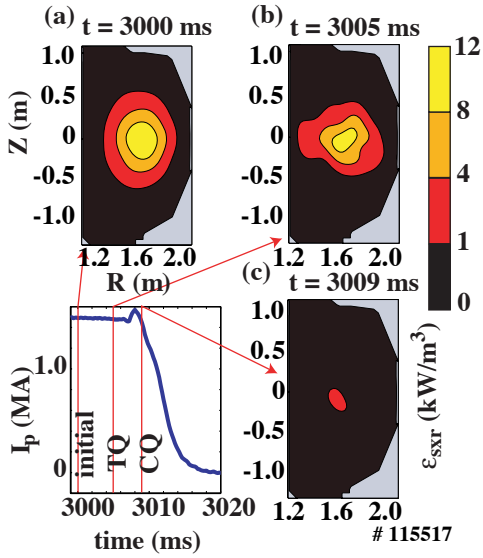

Fig. 10. Soft x-ray emissivity contours before disruption, during thermal quench, and during current quench for open argon jet disruption.

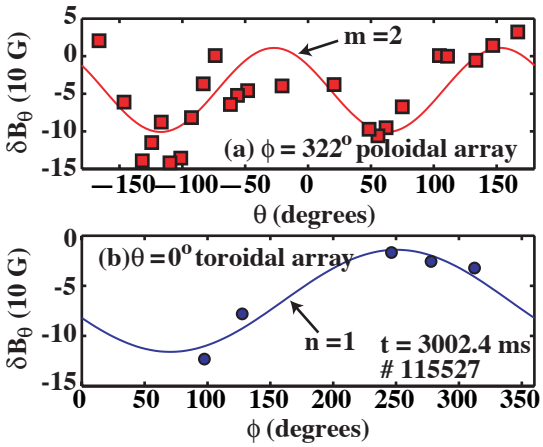

Fig. 11. Perturbed poloidal magnetic field δB_θ measured at vessel wall during the thermal quench of an open neon jet disruption.

7. Discussion

The ideal gas jet mitigation scheme should deposit a large number of radiating impurities uniformly throughout the plasma volume to provide a uniform radiative collapse, avoid MHD-driving pressure and current gradients, and collisionally suppress the amplification of runaway electrons. In these experiments, the neutral deposition is far from ideal, remaining fairly localized to the injection port. In ITER, the situation will probably be similar: the ablation pressure at the edge of the pedestal will be of order 100 atm, so designing a gas jet to penetrate into the core of ITER will be challenging, requiring an improvement of three orders of magnitude over the present DIII-D gas jet.

Despite this non-ideal deposition of neutrals, the gas puff disruptions studied here show good shutdown characteristics: nearly unity TQ radiated power fraction, small divertor heat loads, and small divertor vessel currents. Also, runaway electron generation is small: the runaways appear to remain confined to a small central channel, carry only a small fraction of the plasma current, and dissipate after several ms.

An encouraging aspect of this work is the ability of the large MHD to bring the plasma core into good thermal contact with the injected impurities without simultaneously causing large conducted heat loads to the wall and divertor; *i.e.* the MHD appears to preferentially deposit heat into the radiating impurity impurities, rather than the walls. This suggests that rapid core shutdown could be obtained in ITER even without core penetration of the jet impurities. However, this work indicates that prediction of gas jet behavior in ITER will require integrated modeling of impurity ion and neutral dynamics while including the MHD response of the plasma.

Acknowledgments

Discussions with G. Antar, J. Boedo, B. Bray, T. Luce, S. Luckhardt, S. Pigarov, and R. Pitts and the experimental assistance of the DIII-D team are acknowledged. This work was supported by U.S. DOE Grants DE-FG03-95ER54294, DE-FG02-89ER53297, and Contracts DE-AC03-99ER54463, DE-AC05-00OR22275, and W-7405-ENG-48.

References

[1] SHIMOMURA, Y., Nucl. Fusion **41**, 316 (2001).
[2] GRANETZ, R.S., HUTCHINSON, I.H., J. Sorci, *et al.*, Nucl. Fusion **36**, 545 (1996).
[3] GILLIGAN, J., *et al.*, J. Nucl. Mater. **176-177**, 779 (1990).
[4] WHYTE, D.G., JERNIGAN, T.C., HUMPHREYS, D.A., *et al.*, J. Nucl. Mater. **313**, 1239 (2003).
[5] PAUTASSO, G., *et al.*, Nucl. Fusion **36**, 1291 (1996).
[6] YOSHINO, R., *et al.*, Plasma Phys. Control Fusion **39**, 313 (1997).
[7] TAYLOR, P.L., *et al.*, Phys. Plasmas **6**, 1872 (1999).
[8] TIMOKHIN, V.M., *et al.*, Plasma Phys. Rep. **27**, 181 (2001).
[9] FINKEN, K.H., *et al.*, Nucl. Fusion **41**, 1651 (2001).
[10] BAKHTIARI, M. KAWANO, Y., TAMIA, H., *et al.*, Nucl. Fusion **42**, 1197 (2002).
[11] RICCARDO, V., *et al.*, Plasmas Phys. Control. Fusion **44**, 905 (2002).
[12] HOPCRAFT, K.I., SYKES, A., and TURNER, M.F., Nucl. Fusion **28**, 1265 (1988).
[13] LUXON, J.L., Nucl. Fusion **42**, 614 (2002).
[14] GRAY, D.S., HOLLMANN, E.M., LUCKHARDT, S.C., *et al.*, to appear in Rev. Sci. Instrum. (2004).
[15] MURPHY, H. and MILLER, D., J. Phys. Chem. **88**, 4474 (1984).
[16] ROZHANSKY, V., SENICHENKOV, I., VESELOVA, I., *et al*, in Proc. 28th EPS Conf. Contr. Fusion Plasma Phys., London (2004).
[17] PARKS, P.B., ROSENBLUTH, M.N., PUTVINSKI, S.V., and EVANS, T.E., Fusion Technol. **35**, 267 (1999).
[18] HOLLMANN, E.M., GRAY, D.S., WHYTE, D.G., *et al.*, Phys. Plasmas **10**, 2863 (2003).
[18] HOLLMANN, E.M., GRAY, D.S., BROOKS, N.H., *et al.*, in Proc. 28th EPS Conf. Contr. Fusion Plasma Phys., London (2004).
[20] CARRERAS, B., HICKS, H.R., HOLMES, J.A., and WADDELL, B.V., Phys. Fluids **23**, 1811 (1980).
[21] WESSON, J., *Tokamaks 2nd Ed.* (Oxford University Press,Oxford, 1997).
[22] KLEVA, R.G. and DRAKE, J.F., Phys. Fluids B **3**, 372 (1991).